Please verify that (1) all pages are present, (2) all figures are correct, (3) all fonts and special characters are correct, and (4) all text and figures fit within the red margin lines shown on this review document. Complete formatting information is available at http://SPIE.org/manuscripts

Return to the Manage Active Submissions page at http://spie.org/submissions/tasks.aspx and approve or disapprove this submission. Your manuscript will not be published without this approval. Please contact authorhelp@spie.org with any questions or concerns.

Hyperspectral Structured-Illumination Reflectance Imaging for Early-Stage Rot Detection in Blueberries

Ashfak Yeafi[a], Yuzhen Lu[a], Stephanie Rett-Cadman[b], Joshua Vander Weide[b], and Timothy D. Miles[c]

[a]Department of Biosystems and Agricultural Engineering, Michigan State University, East Lansing, MI 48824, United States
[b]Department of Horticulture, Michigan State University, East Lansing, MI 48824, United States
[c]Department of Plant, Soil and Microbial Sciences, Michigan State University, East Lansing, MI 48824, United States

ABSTRACT

Early-stage rot detection in blueberries is important for postharvest quality control, but it remains challenging because infected fruit may show subtle or no visible symptoms during the initial stage of decay. This study investigated a hyperspectral structured-illumination reflectance imaging (SIRI) system for non-destructive detection of blueberry rot. A total of 144 blueberries, including healthy control samples and fruit inoculated with pathogens associated with anthracnose fruit rot and botrytis fruit rot, were monitored over five scanning days, resulting in 720 observations labeled as healthy, moderately rotten, or severely rotten. Phase-shifted hyperspectral images were acquired at five structured-illumination spatial frequencies and demodulated into direct component (DC) and amplitude component (AC) images. Spectral and spatial features were extracted from individual berry regions and evaluated using machine learning classifiers, including random forest, logistic regression, support vector machine, k-nearest neighbors, and regularized linear discriminant analysis (RLDA). The three rot classes showed clear spectral differences, particularly in the near-infrared region, where healthy berries generally exhibited higher reflectance than rotten samples. AC-based features provided better class separation and classification performance than DC-based features, indicating the benefit of structured illumination for enhancing rot detection. Among the evaluated classifiers, RLDA achieved the best overall performance, with the highest accuracy of 94.2% obtained at the 0.030 cycles/mm spatial frequency. These results suggest that hyperspectral SIRI, especially using AC spectral features at an intermediate frequency, is a promising approach for early-stage blueberry rot detection.

Keywords: Blueberry, early-stage rot, structured-illumination, hyperspectral imaging, machine learning

1. INTRODUCTION

Blueberries are a high-value fruit crop with substantial economic importance in the United States (U.S.). In 2024, U.S. cultivated blueberry production reached a record 789.5 million pounds with a value of $1.15 billion, while wild blueberry production added 90.8 million pounds valued at $49.3 million; approximately 55% of cultivated blueberries were destined for the fresh market [1]. For fresh-market blueberries, the U.S. grade standards require fruit to be free from serious defects and damage, including visible decay, shriveling, scars, and broken skins [2,3]. Failure to identify and remove defective fruit can reduce marketability, shorten shelf life, and increase postharvest economic losses.

Postharvest rot is one of the major quality challenges for blueberries. Blueberries are susceptible to multiple fungal diseases during production, storage, and distribution, including anthracnose fruit rot (AFR) and botrytis fruit rot (BFR) [4,5]. These diseases are particularly difficult to manage because infections may remain latent before becoming visible, and symptom development can continue during storage or transport under favorable

*Correspondence: Yuzhen Lu (luyuzhen@msu.edu)

SPIE USE: ____ DB Check, ____ Prod Check, Notes:

Please verify that (1) all pages are present, (2) all figures are correct, (3) all fonts and special characters are correct, and (4) all text and figures fit within the red margin lines shown on this review document. Complete formatting information is available at http://SPIE.org/manuscripts

Return to the Manage Active Submissions page at http://spie.org/submissions/tasks.aspx and approve or disapprove this submission. Your manuscript will not be published without this approval. Please contact authorhelp@spie.org with any questions or concerns.

environmental conditions [5]. Once decayed fruit enter a packing or storage lot, they may accelerate lot-level deterioration and reduce the quality of otherwise marketable fruit. Therefore, early identification and removal of affected berries are critical for protecting fresh-market quality.

Early-stage rot detection is difficult because of the lack of clear visual symptoms. At this incipient stage, berries can appear acceptable to human inspectors even though subtle surface, near-surface, or internal tissue changes have already started. Manual sorting remains labor-intensive, subjective, and limited by operator fatigue and the visibility of defects. Conventional color or RGB (red-green-blue) imaging has been explored for blueberry orientation and disease detection [6]; however, many blueberry defects are difficult to distinguish using color information alone because the fruit skin is naturally dark and the contrast between early defects and normal tissue can be low [3]. These limitations motivate the development of more advanced optical methods that can detect early quality deterioration before severe external symptoms are present.

Hyperspectral imaging is a powerful tool for non-destructive quality assessment of fruits and vegetables, which combines spatial imaging with wavelength-dependent spectral information [7,8]. In blueberries, previous studies have demonstrated the usefulness of hyperspectral imaging for detecting bruising and disease-related changes in blueberries. Jiang et al. used near-infrared (NIR) hyperspectral reflectance imaging for blueberry bruising detection [9], Zhang et al. showed that hyperspectral transmittance imaging could detect internally bruised blueberries as early as 30 min after mechanical damage [10], and Fan et al. demonstrated the value of data fusion from two hyperspectral systems with complementary spectral ranges for blueberry bruising detection [11]. Huang et al. further investigated visible/near-infrared hyperspectral imaging for early disease detection in blueberries over the 400–1000 nm range [12]. Deng et al. showed that hyperspectral reflectance imaging combined with machine learning could differentiate normal and defective blueberries, with defective samples generally producing lower NIR reflectance than sound samples [3]. Despite these hyperspectral imaging studies, most prior work focused on bruising, general defect detection, or disease classification under conventional reflectance or transmittance sensing configurations.

Structured-illumination reflectance imaging (SIRI) provides an alternative imaging strategy by projecting spatially modulated sinusoidal illumination patterns onto a sample instead of using traditional uniform illumination. In SIRI, multiple phase-shifted pattern images are demodulated into DC and AC images [13]. The DC image is analogous to a conventional uniform illumination-based image, whereas the AC image contains the spatially modulated response and can provide enhanced contrast and resolution [13]. The spatial frequency of the projected pattern controls the balance between image contrast and tissue interrogation depth. Lower spatial frequencies generally interrogate relatively deeper tissue but may provide weaker surface contrast, whereas higher spatial frequencies emphasize shallower tissue responses but may suffer stronger signal attenuation [13]. This frequency-dependent depth-resolving capability makes SIRI effective for detecting subtle surface and near-subsurface defects.

SIRI has shown promise for early decay in horticultural products. Sun et al. demonstrated SIRI-based early decay detection in peaches [14]. Li et al. used SIRI with fast demodulation and improved image processing for identifying early decayed oranges [15], and Cai et al. showed that SIRI combined with texture features and classification models could detect early decayed oranges [16]. More recently, Zhang et al. combined SIRI with deep learning for early decayed orange detection and highlighted the importance of selecting an appropriate spatial frequency [17]. These studies indicate that SIRI can reveal fruit defects that are difficult to observe under conventional imaging, but its application to early-stage blueberry rot detection has yet to be explored.

The combined use of hyperspectral imaging and SIRI may provide complementary benefits for blueberry rot detection. Hyperspectral imaging captures wavelength-dependent changes related to tissue composition, water absorption, pigments, and scattering behavior, while SIRI enhances spatially modulated reflectance information that may be sensitive to surface and near-subsurface changes. However, the relative usefulness of DC and AC hyperspectral features for differentiating healthy, moderately rotten, and severely rotten blueberries has not been studied. In addition, the most informative structured-illumination spatial frequency for early blueberry rot detection is still unknown.

The objective of this study was, therefore, to evaluate a hyperspectral SIRI system for early-stage rot detection in blueberries. Phase-shifted hyperspectral images of healthy and inoculated blueberries were acquired under

Please verify that (1) all pages are present, (2) all figures are correct, (3) all fonts and special characters are correct, and (4) all text and figures fit within the red margin lines shown on this review document. Complete formatting information is available at http://SPIE.org/manuscripts

Return to the Manage Active Submissions page at http://spie.org/submissions/tasks.aspx and approve or disapprove this submission. Your manuscript will not be published without this approval. Please contact authorhelp@spie.org with any questions or concerns.

the structured illumination at multiple spatial frequencies and demodulated into DC and AC hyperspectral images. Spectral and spatial features were extracted from individual berry regions and used to train machine learning classifiers for three-class rot severity classification. DC and AC feature sets were evaluated across spatial frequencies to identify the most informative imaging condition for blueberry rot detection.

2. MATERIALS AND METHODS

2.1 Hyperspectral SIRI system

An in-house hyperspectral SIRI system was used for blueberry imaging, as shown in Figure 1. The system consisted of a digital light projector (DLP) (LightCrafter 6500, DLi, Austin, Texas) for generating programmed sinusoidal illumination patterns, a broadband quartz tungsten halogen (QTH) light source coupled with a liquid light guide for illumination delivery, and a hyperspectral camera (Specim IQ, Oulu, Finland) for reflectance image acquisition. The camera employs internal scanning mechanisms for hyperspectral image acquisition, requiring either no sample or camera movement, and it operates in the visible and NIR range from 400 to 1000 nm, with 204 spectral bands, a spectral resolution of approximately 7 nm, and a spatial image size of 512 × 512 pixels.

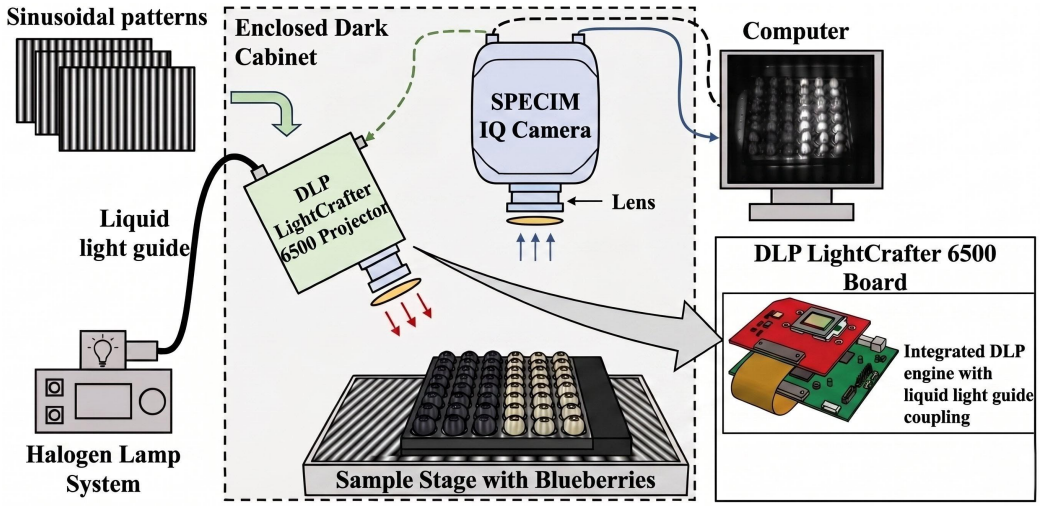

Figure 1. Hyperspectral structured-illumination reflectance imaging system used for blueberry rot detection. The system included a DLP for sinusoidal pattern projection, a QTH light source coupled with a liquid light guide, and a hyperspectral camera for image acquisition in the 400–1000 nm wavelength range.

During imaging, the camera was positioned perpendicularly downward at approximately 30 cm above the sample surface, providing a pixel resolution of about 0.07 mm/pixel. The projected structured illumination covered an area of approximately 14 cm × 7 cm over the blueberry sample tray. The projector generated sinusoidal patterns at selected spatial frequencies, and the hyperspectral camera recorded the reflected pattern response from the blueberry samples. This configuration enabled the acquisition of both wavelength-dependent reflectance information and structured-illumination responses from the same fruit. Compared with conventional hyperspectral reflectance imaging, the SIRI configuration provided additional AC information associated with the spatially modulated component of the reflected light.

2.2 Blueberry samples and experimental dataset

This study used a total of 144 blueberry samples, including 48 healthy reference (control) berries and 96 inoculated berries. The inoculated berries were prepared using fungal pathogens associated with two postharvest blueberry fruit rot diseases, i.e., AFR and BFR. The two diseases are important causes of blueberry fruit decay and can remain latent or continue developing during postharvest storage, making early detection important for fresh-market quality control [4, 5].

The samples were monitored over five scanning days, with scans performed at one-day intervals to observe rot development. On each scanning day, every berry was visually examined and assigned to one of three rot-severity

SPIE USE: ____ DB Check, ____ Prod Check, Notes:

Please verify that (1) all pages are present, (2) all figures are correct, (3) all fonts and special characters are correct, and (4) all text and figures fit within the red margin lines shown on this review document. Complete formatting information is available at http://SPIE.org/manuscripts

Return to the Manage Active Submissions page at http://spie.org/submissions/tasks.aspx and approve or disapprove this submission. Your manuscript will not be published without this approval. Please contact authorhelp@spie.org with any questions or concerns.

classes: healthy, moderately rotten, or severely rotten. This imaging procedure produced 720 total observations, consisting of 258 healthy, 196 moderately rotten, and 266 severely rotten observations. Representative blueberry samples and structured-illumination patterns are shown in Figure 2, and the corresponding training/testing split is summarized in Table 1.

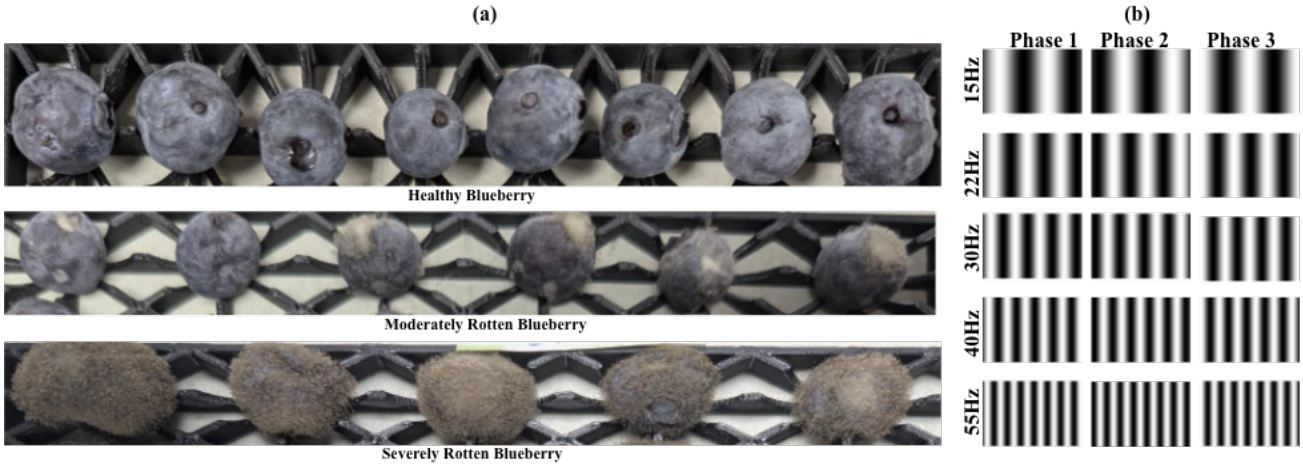

Figure 2. Representative blueberry samples and structured-illumination pattern set used in this study. (a) Example blueberry observations labeled as healthy, moderately rotten, and severely rotten. (b) Three phase-shifted sinusoidal patterns generated at five projector pattern settings.

Table 1. Class distribution of blueberry observations used for training and testing.

Class	Total observations	Training observations	Testing observations
Healthy	258	180	78
Moderately rotten	196	137	59
Severely rotten	266	186	80
Total	720	503	217

The dataset was divided into training and testing subsets using a 70/30 split. The training set contained 503 observations, including 180 healthy, 137 moderately rotten, and 186 severely rotten observations. The testing set contained 217 observations, including 78 healthy, 59 moderately rotten, and 80 severely rotten observations. These subsets were used for model training and performance evaluation of blueberry rot-severity classification.

2.3 Image acquisition and demodulation

Blueberries were imaged under three phase-shifted sinusoidal illumination patterns at each spatial frequency. Five calibrated spatial frequencies were used: 0.015, 0.022, 0.030, 0.040, and 0.055 cycles/mm. In the projector pattern file names and figure labels, these settings were denoted as 15, 22, 30, 40, and 55 Hz, respectively(Figure 2b). For each spatial frequency f_k, three hyperspectral pattern images were acquired with phase offsets of 0, $2\pi/3$, and $4\pi/3$.

For a given wavelength λ and spatial frequency f_k, the three acquired phase-shifted images can be written as

$$I_1(x, y, \lambda; f_k) = I_{\mathrm{DC}}(x, y, \lambda; f_k) + I_{\mathrm{AC}}(x, y, \lambda; f_k) \cos(2\pi f_k x), \tag{1}$$

$$I_2(x, y, \lambda; f_k) = I_{\mathrm{DC}}(x, y, \lambda; f_k) + I_{\mathrm{AC}}(x, y, \lambda; f_k) \cos\left(2\pi f_k x + \frac{2\pi}{3}\right), \tag{2}$$

$$I_3(x, y, \lambda; f_k) = I_{\mathrm{DC}}(x, y, \lambda; f_k) + I_{\mathrm{AC}}(x, y, \lambda; f_k) \cos\left(2\pi f_k x + \frac{4\pi}{3}\right), \tag{3}$$

Please verify that (1) all pages are present, (2) all figures are correct, (3) all fonts and special characters are correct, and (4) all text and figures fit within the red margin lines shown on this review document. Complete formatting information is available at http://SPIE.org/manuscripts

Return to the Manage Active Submissions page at http://spie.org/submissions/tasks.aspx and approve or disapprove this submission. Your manuscript will not be published without this approval. Please contact authorhelp@spie.org with any questions or concerns.

where I_1, I_2, and I_3 denote the three phase-shifted hyperspectral pattern images; (x, y) denotes spatial coordinates; λ denotes wavelength; and f_k denotes the structured-illumination spatial frequency.

The DC and AC hyperspectral images were recovered using the conventional three-phase demodulation method [13]. The DC and AC images were calculated as follows:

$$I_{\mathrm{DC}}(x, y, \lambda; f_k) = \frac{I_1(x, y, \lambda; f_k) + I_2(x, y, \lambda; f_k) + I_3(x, y, \lambda; f_k)}{3}, \tag{4}$$

$$I_{\mathrm{AC}}(x, y, \lambda; f_k) = \frac{\sqrt{2}}{3}\sqrt{(I_1 - I_2)^2 + (I_2 - I_3)^2 + (I_3 - I_1)^2}, \tag{5}$$

where the dependence on $(x, y, \lambda; f_k)$ is omitted in Eq. (5) for compact notation. The DC image represents the average reflectance-like response, while the AC image represents the spatially modulated reflectance amplitude. Because AC images are sensitive to the spatial frequency of the projected pattern, they can emphasize surface and near-subsurface information differently from DC images [13].

2.4 Berry segmentation and feature extraction

For each spatial frequency, the demodulated DC and AC hyperspectral images were processed to extract sample-wise features from individual blueberries. Each berry was segmented from the demodulated hyperspectral data to define a fruit region of interest. The segmentation masks were used to exclude the background and neighboring berries from feature extraction, and segmented berry regions were visually checked to remove obvious segmentation errors before spectral and spatial features were calculated. Spectral features were extracted by calculating the mean spectrum within each segmented berry region. For the ith berry region Ω_i, the mean spectral feature at wavelength λ_m was computed as

$$\bar{R}_i(\lambda_m) = \frac{1}{|\Omega_i|}\sum_{(x,y)\in\Omega_i} R(x, y, \lambda_m), \tag{6}$$

where $R(x, y, \lambda_m)$ denotes either the DC or AC response at wavelength λ_m, and $|\Omega_i|$ is the number of pixels in the segmented region. This produced a wavelength-dependent spectral vector for each berry observation, separately for DC and AC data.

Spatial features were also extracted from each fruit segment to describe shape and texture characteristics. These descriptors included Hu moments, Haralick texture features, local binary patterns (LBP), Gabor features, and binarized statistical image features (BSIF). Hu moments provide shape-related invariant features [18]; Haralick features characterize gray-level co-occurrence texture patterns [19]; LBP features describe local intensity patterns [20]; Gabor features capture oriented texture responses [21]; and BSIF features provide a learned filter-based texture representation [22]. The extracted spatial feature set consisted of 7 Hu features, 28 Haralick features, 58 LBP features, 67 Gabor features, and 256 BSIF features, as summarized in Table 2. Spectral-only, spatial-only, and combined spectral-spatial feature sets were then prepared for classification. The overall feature extraction and classification workflow is summarized in Figure 3.

Table 2. Feature groups extracted from each segmented blueberry observation.

Feature group	Number of features	Main information represented
Mean spectrum	204	Wavelength-dependent DC or AC response
Hu moments	7	Global shape characteristics
Haralick features	28	Gray-level co-occurrence texture
Local binary patterns	58	Local intensity texture patterns
Gabor features	67	Oriented texture responses
BSIF features	256	Filter-based statistical image texture

SPIE USE: ____ DB Check, ____ Prod Check, Notes:

Please verify that (1) all pages are present, (2) all figures are correct, (3) all fonts and special characters are correct, and (4) all text and figures fit within the red margin lines shown on this review document. Complete formatting information is available at http://SPIE.org/manuscripts

Return to the Manage Active Submissions page at http://spie.org/submissions/tasks.aspx and approve or disapprove this submission. Your manuscript will not be published without this approval. Please contact authorhelp@spie.org with any questions or concerns.

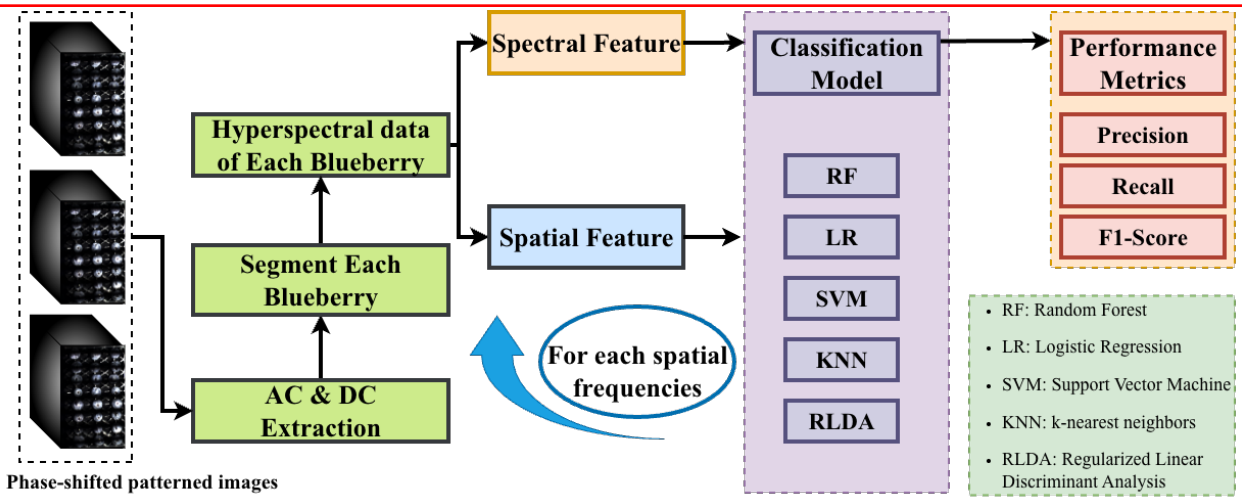

Figure 3. Overall workflow for blueberry rot detection using hyperspectral SIRI. Phase-shifted hyperspectral pattern images were demodulated into DC and AC images, followed by individual berry segmentation, spectral and spatial feature extraction, machine-learning classification, and performance evaluation.

2.5 Machine-learning classification and performance evaluation

Machine-learning models were trained to classify blueberry observations into three classes, i.e., healthy, moderately rotten, and severely rotten. Five classifiers were evaluated: random forest (RF), logistic regression (LR), support vector machine (SVM), k-nearest neighbors (KNN), and regularized linear discriminant analysis (RLDA). These models were selected to compare tree-based, linear, margin-based, instance-based, and discriminant-analysis approaches. RF is effective for nonlinear feature interactions and tabular data [23]; SVM provides margin-based classification [24]; KNN classifies samples based on local neighborhood similarity [25]; and RLDA improves conventional linear discriminant analysis by regularizing covariance estimation, which can be useful when spectral features are correlated [26]. Model implementation and preprocessing followed standard machine-learning practice using normalized feature inputs.

For each spatial frequency, separate models were trained using DC and AC features. Spectral-only, spatial-only, and combined spectral-spatial features were compared to evaluate the relative contribution of wavelength-dependent and texture-based information. Classification performance was evaluated using precision, recall, F1-score, and overall accuracy. For a given class c, precision, recall, and F1-score were calculated as follows:

$$\text{Precision}_c = \frac{\text{TP}_c}{\text{TP}_c + \text{FP}_c}, \tag{7}$$

$$\text{Recall}_c = \frac{\text{TP}_c}{\text{TP}_c + \text{FN}_c}, \tag{8}$$

$$\text{F1}_c = \frac{2 \times \text{Precision}_c \times \text{Recall}_c}{\text{Precision}_c + \text{Recall}_c}, \tag{9}$$

where TP_c, FP_c, and FN_c denote the numbers of true positive, false positive, and false negative predictions for class c, respectively. Overall classification accuracy was calculated as

$$\text{Accuracy} = \frac{N_{\text{correct}}}{N_{\text{total}}}, \tag{10}$$

where N_{correct} is the number of correctly classified observations and N_{total} is the total number of testing observations. The effect of structured-illumination frequency was then analyzed by comparing model performance across the five frequency settings.

SPIE USE: ____ DB Check, ____ Prod Check, Notes:

Please verify that (1) all pages are present, (2) all figures are correct, (3) all fonts and special characters are correct, and (4) all text and figures fit within the red margin lines shown on this review document. Complete formatting information is available at http://SPIE.org/manuscripts

Return to the Manage Active Submissions page at http://spie.org/submissions/tasks.aspx and approve or disapprove this submission. Your manuscript will not be published without this approval. Please contact authorhelp@spie.org with any questions or concerns.

3. RESULTS AND DISCUSSION

3.1 Spectral response of blueberry rot classes

Representative spectral responses at the spatial frequency of 0.030 cycles/mm are shown in Figure 4. The mean spectra of healthy, moderately rotten, and severely rotten blueberries showed clear class-dependent differences across the 400–1000 nm wavelength range. For all three classes, reflectance remained relatively low in the visible region and increased rapidly beyond approximately 700 nm, reaching a broad high-reflectance region in the near-infrared range before decreasing near the longer wavelengths. This general spectral behavior is consistent with previous hyperspectral blueberry studies, which reported more prominent differences between sound and defective samples in the NIR region than in the visible region [3].

The strongest separation among the three classes occurred in the NIR region. Healthy blueberries generally showed higher reflectance than rotten ones, while moderately and severely rotten samples showed lower reflectance responses. This trend suggests that rot progression altered the optical response of blueberry tissue. Such changes may be associated with tissue softening, cellular breakdown, changes in water-related absorption, and increased scattering or absorption differences in affected tissue. Because these changes are more evident spectrally than visually, the NIR separation provides an important basis for machine-learning-based rot classification.

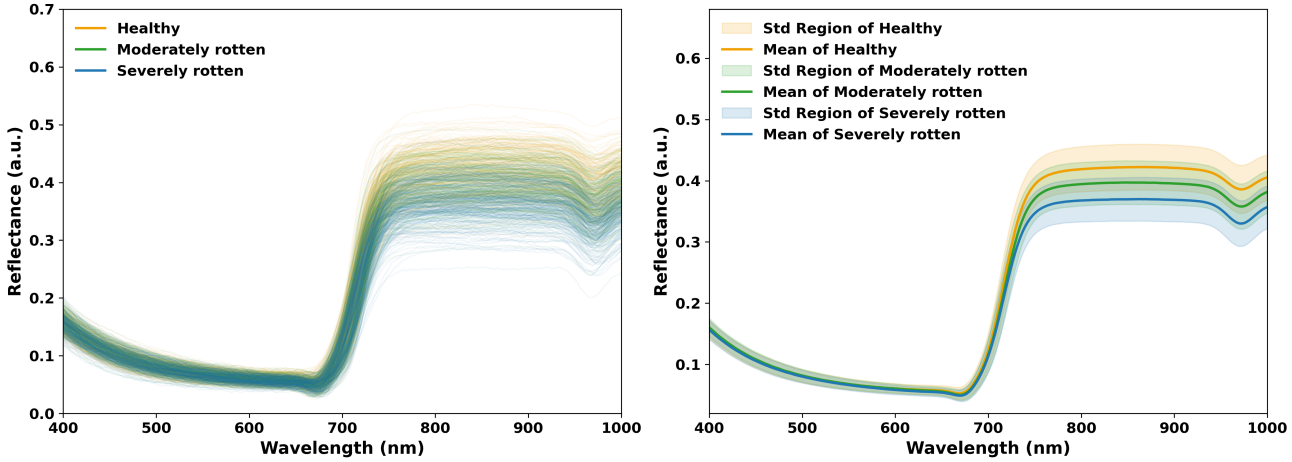

Figure 4. Representative spectral responses of healthy, moderately rotten, and severely rotten blueberries at the 0.030 cycles/mm structured-illumination setting. (a) Individual sample spectra showing within-class variation. (b) Mean spectra with standard-deviation regions for each class. The strongest class-dependent differences were observed in the NIR region, where healthy blueberries generally exhibited higher reflectance than rotten samples.

3.2 PCA analysis of DC and AC spectral features

Principal component analysis (PCA) was applied to the DC and AC spectral features to visualize the distribution of blueberry observations in a reduced feature space. As shown in Figure 5, both DC and AC features produced class-dependent clustering trends. Healthy observations tended to separate from rotten observations, while moderate and severe rot classes showed partial overlap. This overlap is reasonable because rot development is gradual, and visual class labels represent severity stages rather than sharply separated biological states.

Compared with DC features, AC spectral features showed relatively clearer class separation. This observation agrees with the expected behavior of SIRI. In SIRI, AC images can improve contrast and resolution by emphasizing the spatially modulated portion of the reflected signal and reducing the effect of diffuse background scattering [13]. For early-stage blueberry rot detection, this contrast enhancement is useful because affected tissue may show only subtle surface or near-subsurface optical differences. The PCA result suggests that AC hyperspectral features provide more discriminative information than conventional DC-like reflectance features.

Please verify that (1) all pages are present, (2) all figures are correct, (3) all fonts and special characters are correct, and (4) all text and figures fit within the red margin lines shown on this review document. Complete formatting information is available at http://SPIE.org/manuscripts

Return to the Manage Active Submissions page at http://spie.org/submissions/tasks.aspx and approve or disapprove this submission. Your manuscript will not be published without this approval. Please contact authorhelp@spie.org with any questions or concerns.

Figure 5. PCA visualization of spectral features extracted from blueberry observations at the 0.030 cycles/mm spatial frequency. (a) DC spectral features. (b) AC spectral features. Both feature types showed class-dependent clustering, while AC features provided relatively clearer separation between healthy and rotten blueberries.

3.3 Classification performance of machine-learning models

The classification performance of RF, LR, SVM, KNN, and RLDA models is compared in Figure 6, and the corresponding accuracy values are summarized in Table 3. Overall, spectral features produced stronger classification performance than spatial features for both DC and AC data. This indicates that wavelength-dependent reflectance information was more discriminative for blueberry rot-severity classification than texture and shape descriptors alone. This finding is consistent with earlier blueberry hyperspectral work, where spectral features produced stronger separation and classification performance than spatial features for distinguishing normal and defective blueberries [3]. Spatial features still provided complementary visual information, but their performance was limited by the subtle and progressive appearance of early rot symptoms.

Table 3. Classification accuracy (%) of machine-learning models using DC and AC feature sets at the 0.030 cycles/mm structured-illumination setting.

Model	DC features			AC features		
	Spectral	Spatial	Combined	Spectral	Spatial	Combined
RF	82.4	78.6	80.7	84.0	80.2	82.1
LR	84.9	76.8	82.4	86.3	78.4	84.0
SVM	89.0	84.1	87.2	90.8	85.4	88.6
KNN	80.7	74.9	78.5	82.1	76.3	80.0
RLDA	89.8	83.2	89.1	**94.2**	84.7	91.6

AC-based features generally outperformed DC-based features across the tested classifiers. As shown in Table 3, RLDA achieved the highest overall performance, with the best accuracy of 94.2% using AC spectral features at the 0.030 cycles/mm structured-illumination setting. SVM also showed strong performance, reaching 90.8% accuracy with AC spectral features. Combined spectral-spatial features were competitive in some cases, especially for RLDA, where AC combined features achieved 91.6% accuracy. However, feature concatenation did not consistently improve performance beyond the best spectral-feature results. This suggests that wavelength-dependent spectral information was the dominant source of discriminative information for the current dataset.

The strong performance of RLDA suggests that the extracted spectral features contained class-separable information that could be modeled effectively using a regularized linear decision boundary. This is practically attractive because linear discriminant models are computationally efficient and easier to implement than many

Please verify that (1) all pages are present, (2) all figures are correct, (3) all fonts and special characters are correct, and (4) all text and figures fit within the red margin lines shown on this review document. Complete formatting information is available at http://SPIE.org/manuscripts

Return to the Manage Active Submissions page at http://spie.org/submissions/tasks.aspx and approve or disapprove this submission. Your manuscript will not be published without this approval. Please contact authorhelp@spie.org with any questions or concerns.

high-capacity nonlinear models. Therefore, the combination of AC spectral features and RLDA provided the most effective classification strategy among the tested approaches.

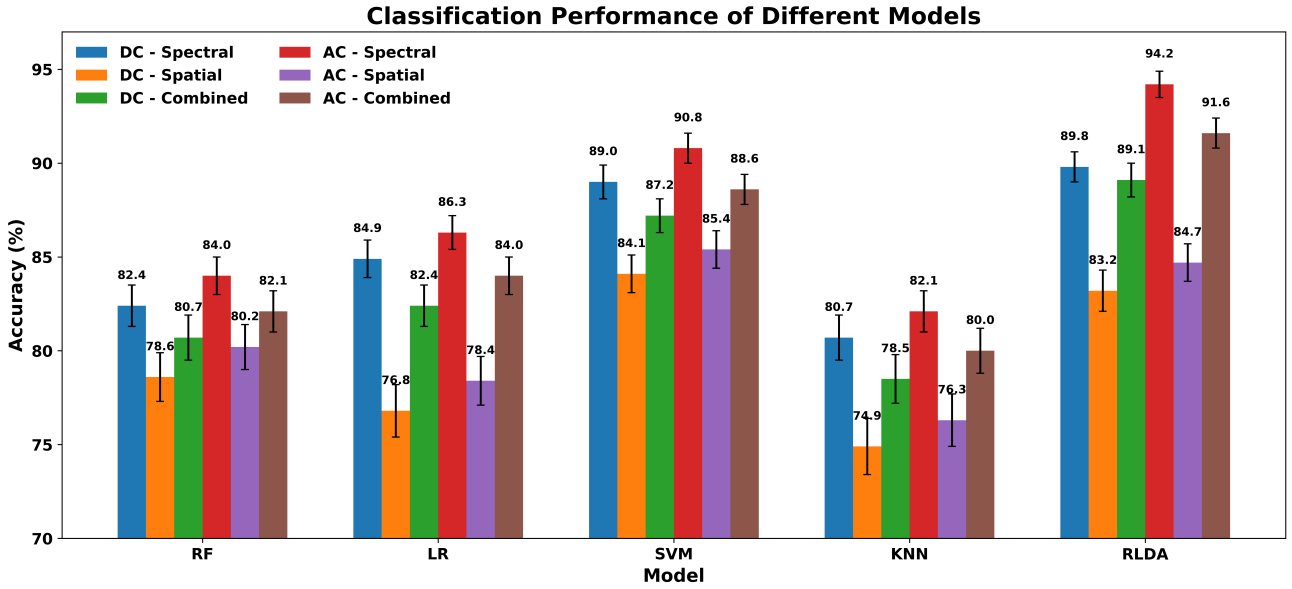

Figure 6. Classification performance of different machine-learning models using DC and AC spectral, spatial, and combined features at the 0.030 cycles/mm structured-illumination setting. Spectral features generally outperformed spatial features, AC-based features performed better than DC-based features, and RLDA achieved the highest overall accuracy.

3.4 Effect of spatial frequency

The effect of structured-illumination spatial frequency was evaluated using RLDA models trained on DC and AC spectral features. As shown in Figure 7, DC-based classification accuracy remained relatively stable across the five frequencies. This is expected because the DC component is computed as the average of phase-shifted images and is closer to a conventional reflectance response. In contrast, AC-based classification accuracy changed more noticeably with spatial frequency. The best AC-based result was obtained at the intermediate frequency of 0.030 cycles/mm, corresponding to the 30 Hz projector setting, while performance decreased at both lower and higher frequencies.

This frequency-dependent behavior is consistent with the depth-resolving nature of SIRI. Lower spatial frequencies can probe relatively deeper tissue but may provide weaker contrast for subtle surface or near-subsurface changes. Higher spatial frequencies can enhance shallow surface contrast, but they also experience stronger attenuation and may reduce the signal-to-noise ratio of AC images [13]. The superior result at the intermediate frequency suggests that 0.030 cycles/mm provided a useful balance between contrast enhancement and tissue interrogation depth for early-stage blueberry rot detection. This finding is important because optimal spatial frequency is sample- and defect-dependent; a frequency that works well for one fruit or defect type may not be optimal for small, dark-skinned fruit such as blueberries.

3.5 Implications and limitations

The results indicate that hyperspectral SIRI provides useful information for differentiating healthy, moderately rotten, and severely rotten blueberries. The advantage of AC spectral features suggests that structured illumination can reveal subtle optical changes that are less apparent in DC images. This highlights the strength of SIRI for postharvest grading because early rot symptoms may be difficult to detect by visual inspection or conventional imaging. The frequency comparison further indicates that careful selection of the illumination pattern is necessary for maximizing the effectiveness of SIRI-based inspection.

This study has limitations that should be considered when interpreting the results. First, the dataset included repeated observations of the same berries across multiple scanning days. Although this design is useful for

SPIE USE: ____ DB Check, ____ Prod Check, Notes:

Please verify that (1) all pages are present, (2) all figures are correct, (3) all fonts and special characters are correct, and (4) all text and figures fit within the red margin lines shown on this review document. Complete formatting information is available at http://SPIE.org/manuscripts

Return to the Manage Active Submissions page at http://spie.org/submissions/tasks.aspx and approve or disapprove this submission. Your manuscript will not be published without this approval. Please contact authorhelp@spie.org with any questions or concerns.

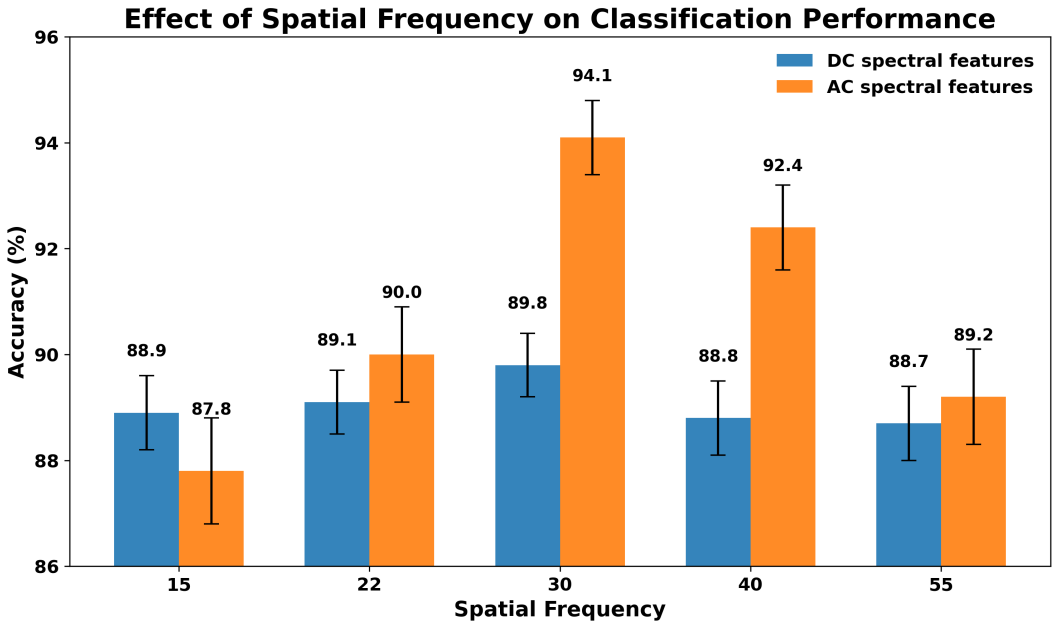

Figure 7. Effect of structured-illumination frequency on RLDA classification performance using DC and AC spectral features. DC-based accuracy remained relatively stable across frequency settings, while AC-based accuracy was more frequency dependent. The best performance was obtained at the intermediate frequency setting of 0.030 cycles/mm.

observing rot progression, future validation should include berry-level or batch-level splits to more rigorously evaluate model generalization. Second, the dataset size was relatively limited, and the samples were labeled by visual inspection. Future work should include larger sample sets, more cultivars, controlled storage conditions, and additional reference measurements to better characterize rot progression. Finally, this study evaluated hand-crafted spectral and spatial features with traditional machine-learning models. Deep learning, feature selection, wavelength optimization, and model-level fusion may further improve robustness and support future online inspection applications.

4. CONCLUSION

This study evaluated a hyperspectral SIRI framework for early-stage rot detection in blueberries. Phase-shifted hyperspectral images were demodulated into DC and AC images, and spectral and spatial features were extracted from individual berry observations for machine-learning-based classification. The results showed that healthy, moderately rotten, and severely rotten blueberries exhibited clear spectral differences, particularly in the near-infrared region. Healthy blueberries generally showed higher reflectance than rotten blueberries, indicating that rot progression altered the spectral response of fruit tissue. Among the evaluated feature types, spectral features were more discriminative than spatial features for classifying blueberry rot severity. AC-based features also provided better class separation and classification performance than DC-based features, supporting the usefulness of structured illumination for enhancing subtle surface and near-subsurface optical differences. Among the tested classifiers, RLDA achieved the best overall performance, with the highest accuracy of 94.2% obtained using AC spectral features at the 0.030 cycles/mm setting, corresponding to the 30 Hz projector setting. The frequency comparison showed that DC-based classification performance remained relatively stable across the tested settings, whereas AC-based performance was more frequency dependent. The best result at the intermediate frequency setting suggests that an appropriate balance between contrast enhancement and tissue interrogation depth is important for early blueberry rot detection. Overall, the findings indicate that hyperspectral SIRI is a promising non-destructive approach for detecting early-stage rot in blueberries.

Please verify that (1) all pages are present, (2) all figures are correct, (3) all fonts and special characters are correct, and (4) all text and figures fit within the red margin lines shown on this review document. Complete formatting information is available at http://SPIE.org/manuscripts

Return to the Manage Active Submissions page at http://spie.org/submissions/tasks.aspx and approve or disapprove this submission. Your manuscript will not be published without this approval. Please contact authorhelp@spie.org with any questions or concerns.

ACKNOWLEDGMENTS

This research was supported by the USDA National Institute of Food and Agriculture, Specialty Crop Research Initiative (Project No. 2023-51181-41322).

REFERENCES

[1] USDA Economic Research Service, "Most cultivated blueberries are destined for the fresh market, while wild blueberries are bound for processing," (2025). Charts of Note, September 18, 2025. Accessed 2026-05-15.

[2] USDA Agricultural Marketing Service, "United states standards for grades of blueberries," (1995). Accessed 2026-05-15.

[3] Deng, B., Lu, Y., and Stafne, E., "Fusing spectral and spatial features of hyperspectral reflectance imagery for differentiating between normal and defective blueberries," *Smart Agricultural Technology* **8**, 100473 (2024).

[4] Bell, S. R., Montiel, L. G. H., Estrada, R. R. G., and Martínez, P. G., "Main diseases in postharvest blueberries, conventional and eco-friendly control methods: A review," *Lwt* **149**, 112046 (2021).

[5] Neugebauer, K. A., Mattupalli, C., Hu, M., Oliver, J. E., VanderWeide, J., Lu, Y., Sullivan, K., Stockwell, V. O., Oudemans, P., and Miles, T. D., "Managing fruit rot diseases of vaccinium corymbosum," *Frontiers in Plant Science* **15**, 1428769 (2024).

[6] Leiva-Valenzuela, G. A. and Aguilera, J. M., "Automatic detection of orientation and diseases in blueberries using image analysis to improve their postharvest storage quality," *Food Control* **33**(1), 166–173 (2013).

[7] Lorente, D., Aleixos, N., Gómez-Sanchis, J., Cubero, S., García-Navarrete, O. L., and Blasco, J., "Recent advances and applications of hyperspectral imaging for fruit and vegetable quality assessment," *Food and Bioprocess Technology* **5**(4), 1121–1142 (2012).

[8] Lu, Y., Huang, Y., and Lu, R., "Innovative hyperspectral imaging-based techniques for quality evaluation of fruits and vegetables: A review," *Applied Sciences* **7**(2), 189 (2017).

[9] Jiang, Y., Li, C., and Takeda, F., "Nondestructive detection and quantification of blueberry bruising using near-infrared (nir) hyperspectral reflectance imaging," *Scientific Reports* **6**(1), 35679 (2016).

[10] Zhang, M., Li, C., Takeda, F., and Yang, F., "Detection of internally bruised blueberries using hyperspectral transmittance imaging," *Transactions of the ASABE* **60**(5), 1489–1502 (2017).

[11] Fan, S., Li, C., Huang, W., and Chen, L., "Data fusion of two hyperspectral imaging systems with complementary spectral sensing ranges for blueberry bruising detection," *Sensors* **18**(12), 4463 (2018).

[12] Huang, Y., Wang, D., Liu, Y., Zhou, H., and Sun, Y., "Measurement of early disease blueberries based on vis/nir hyperspectral imaging system," *Sensors* **20**(20), 5783 (2020).

[13] Lu, Y. and Lu, R., "Structured-illumination reflectance imaging for the detection of defects in fruit: Analysis of resolution, contrast and depth-resolving features," *Biosystems engineering* **180**, 1–15 (2019).

[14] Sun, Y., Lu, R., Lu, Y., Tu, K., and Pan, L., "Detection of early decay in peaches by structured-illumination reflectance imaging," *Postharvest Biology and Technology* **151**, 68–78 (2019).

[15] Li, J., Lu, Y., and Lu, R., "Identification of early decayed oranges using structured-illumination reflectance imaging coupled with fast demodulation and improved image processing algorithms," *Postharvest Biology and Technology* **207**, 112627 (2024).

[16] Cai, Z., Huang, W., Wang, Q., and Li, J., "Detection of early decayed oranges by structured-illumination reflectance imaging coupling with texture feature classification models," *Frontiers in Plant Science* **13**, 952942 (2022).

[17] Zhang, H., Zhang, J., Zhang, Y., Wei, J., Zhan, B., Liu, X., and Luo, W., "Structured-illumination reflectance imaging combined with deep learning for detecting early decayed oranges," *Postharvest Biology and Technology* **217**, 113121 (2024).

[18] Hu, M.-K., "Visual pattern recognition by moment invariants," *IRE transactions on information theory* **8**(2), 179–187 (1962).

[19] Haralick, R. M., Shanmugam, K., and Dinstein, I. H., "Textural features for image classification," *IEEE Transactions on systems, man, and cybernetics* (6), 610–621 (1973).

Please verify that (1) all pages are present, (2) all figures are correct, (3) all fonts and special characters are correct, and (4) all text and figures fit within the red margin lines shown on this review document. Complete formatting information is available at http://SPIE.org/manuscripts

Return to the Manage Active Submissions page at http://spie.org/submissions/tasks.aspx and approve or disapprove this submission. Your manuscript will not be published without this approval. Please contact authorhelp@spie.org with any questions or concerns.

[20] Ojala, T., Pietikäinen, M., and Harwood, D., "A comparative study of texture measures with classification based on featured distributions," *Pattern recognition* **29**(1), 51–59 (1996).

[21] Kumar, A. and Pang, G. K., "Defect detection in textured materials using gabor filters," *IEEE Transactions on industry applications* **38**(2), 425–440 (2002).

[22] Kannala, J. and Rahtu, E., "Bsif: Binarized statistical image features," in [*Proceedings of the 21st international conference on pattern recognition (ICPR2012)*], 1363–1366, IEEE (2012).

[23] Breiman, L., "Random forests," *Machine Learning* **45**, 5–32 (2001).

[24] Cortes, C. and Vapnik, V., "Support-vector networks," *Machine Learning* **20**, 273–297 (1995).

[25] Cover, T. and Hart, P., "Nearest neighbor pattern classification," *IEEE Transactions on Information Theory* **13**(1), 21–27 (1967).

[26] Friedman, J. H., "Regularized discriminant analysis," *Journal of the American Statistical Association* **84**(405), 165–175 (1989).